Mathematical investigation of interfacial property in fiber reinforced model composites

Panagiotis-Nikolaos Tzounis, Leonidas N. Gergidis, Theodore E. Matikas, Antonios Charalambopoulos *

Department of Materials Science and Engineering, University of Ioannina, 45110 Ioannina, Greece

ARTICLE INFO

ABSTRACT

In the current paper, we have investigated the dependence of the effective elastic properties of a composite material on the fiber/matrix interface elastic property. The model composite consists of a single cylindrical fiber embedded in a concentric cylindrical matrix material. A three dimensional mathematical method has been developed connecting the interface properties with the effective axial Young's modulus of the composite structure. Special effort has been devoted to decode information about the quality of the interface by exploiting the information provided by the elastic effective parameters. In particular, the effective modulus vs. stiffness coefficient curves have been generated for Ti/SiC composites. The aforementioned curves reveal the characteristics of the transition from the regime of perfect interface to the realm of complete debonding.

© 2011 Elsevier Ltd. All rights reserved.

1. Introduction

It is commonly accepted that the fiber–matrix interface plays a critical role in the performance of fiber-reinforced composites [1–3]. Various composite performance objectives often impose interface property requirements that may be contradictory in nature. The composite strength and creep resistance in the transverse direction are improved by a stronger interface radial strength, whereas a weak interface is generally desired for crack bridging under fatigue crack growth conditions under longitudinal loading.

Tailoring interface properties is of paramount importance to composite system design. As efforts are made to tailor the interface to satisfy conflicting property requirements, it is desirable to ensure that the interface characterization procedures not only replicate the important modes of interface tensile or shear failure, but also that the test techniques simulate as much as possible the stress states under which the particular mode of failure occurs in actual application. Otherwise, the applicability of the test results for any specific application may become problematic because of the sensitivity of the interface failure conditions on the local stress states and associated additional damage modes and damage interactions. Various techniques are currently available for quantifying the interfacial properties of metal matrix composites. In particular, test methods for measuring the interfacial shear properties of continuously reinforced composites include the effect of radial clamping stress on shear failure of the interface under push-out loading

[4–6], the influence of interface tangential shear failure on the normal separation of the interface under transverse loading [6–8], as well as the fiber fragmentation test.

This study is part of an overall effort to evaluate the influence of the interface on the longitudinal 0° tensile behavior of unidirectional fiber reinforced composites, in the absence of a matrix cracking. Under this type of loading, the interface becomes important only when there is a fiber break, with the interface failure mode assumed as being primarily in shear.

The fiber fragmentation test was developed by Kelly and Tyson [9], who investigated the behavior of brittle tungsten fibers embedded in a copper matrix composite specimen under tension. Elongating the specimens in tension results in fiber breakage into multiple segments. The fiber inside the matrix breaks into increasingly smaller fragments at locations where the axial stress of the fiber reaches its tensile strength. When the fiber breaks, the tensile stress at the location of fracture reduces to zero. Due to the constant shear in the matrix, the tensile stress in the fiber increases almost linearly from its ends to a plateau in longer fragments. The higher the axial strain applied, the more fractures will be caused in the fiber, but at some level the number of breaks will become constant as the fragment length is too short to transfer enough stress from the matrix to the fiber to cause further fragmentation. Although the single-fiber fragmentation test was first performed on metal matrix composites during the early 1960s, the subsequent application of this test was primarily limited to transparent polymer composites due to the ease of their preparation and observation of the fiber fragments using birefringence techniques [10–18].

There has been an interest, however, in the application of this test to model metal matrix composites using various techniques [19–28]. In situ nondestructive observation of single-fiber composites after each of several small strain increments can aid interpretation by providing more complete information than a single destructive observation after fiber fragmentation. Advanced techniques, based on high frequency ultrasound, have been developed for imaging of composite systems under loading with sufficiently large fiber diameters compared to the ultrasonic wavelengths of interrogation, enabling characterization of interfacial elastic property [29–33].

In the present study we simulate the composite fragmentation test under a specific loading condition. We are investigating the case of a model titanium matrix with a SiC fiber. The purpose is the investigation of the influence of elastic properties of the composite components on the interface quality using a novel analytical investigation. We mention here that similar analytical approaches have been introduced in the fundamental papers [34–36]. Our analysis incorporates in addition the analytical background allowing the appearance of discontinuous shearing displacements along the interface of the composite.

2. Theoretical investigation

We consider a concentric cylindrical structure simulating a composite material consisting of a cylindrical core of radius a imbedded in a matrix phase of radius b. Both materials are considered to be isotropic homogeneous elastic media obeying the linearized elasticity theory and fully characterized by the corresponding Lamé constants λ, μ and density ρ. The model geometry is presented in Fig. 1.

For such kind of materials the stress tensor $\tilde{\sigma}$ related to the displacement field $\mathbf{u}$ via the constitutive law

$$\tilde{\sigma} = \mu[\nabla\mathbf{u} + (\nabla\mathbf{u})^T] + \lambda(\nabla \cdot \mathbf{u})\widetilde{\mathscr{I}}. \tag{1}$$

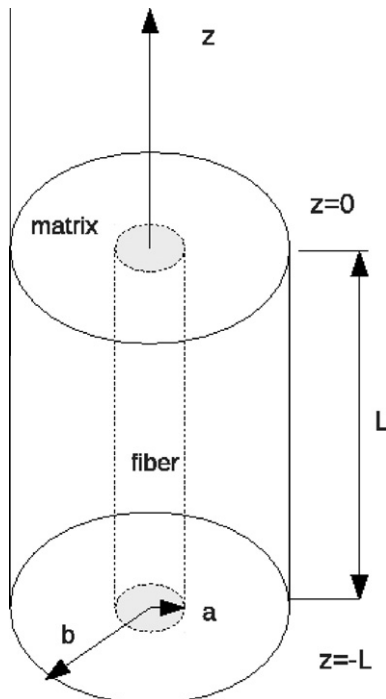The static equilibrium equation

Fig. 1. Model geometry: the outer cylinder represents the matrix (m) while the inner cylinder represents the fiber (f).

$$\nabla \cdot \tilde{\sigma} = \mathbf{0} \tag{2}$$

leads to static Navier's equations of elasticity

$$\mu \, \Delta\mathbf{u} + (\lambda + \mu)\nabla(\nabla \cdot \mathbf{u}) = \mathbf{0}. \tag{3}$$

This is actually a generic formulation and wherever a special notification is made for the specific component of the composite structure, all the involved parameters and fields are denoted by the relevant indices m for matrix and f for fiber.

In the regime of symmetric tension, the evoked fields do not exhibit angular dependence and the elastic displacement fields assume the form

$$\mathbf{u} = u_r(r,z)\hat{\mathbf{r}} + u_z(r,z)\hat{\mathbf{z}} \tag{4}$$

where the radial and axial dependence is explicitly demonstrated. Inserting the expansion (4) into Navier equation, we obtain

$$\mu\left[\frac{\hat{\mathbf{r}}}{r}\frac{\partial}{\partial r}\left(r\frac{\partial u_r}{\partial r}\right) + \frac{\partial^2 u_r}{\partial z^2}\hat{\mathbf{r}} - \frac{1}{r^2}\hat{\mathbf{r}}u_r + \hat{\mathbf{z}}\left(\frac{1}{r}\frac{\partial}{\partial r}\left(r\frac{\partial u_z}{\partial r}\right) + \frac{\partial^2 u_z}{\partial z^2}\right)\right]$$
$$+ (\lambda + \mu)\left[\hat{\mathbf{r}}\frac{\partial^2 u_r}{\partial r^2} - \frac{\hat{\mathbf{r}}}{r^2}u_r + \frac{1}{r}\hat{\mathbf{r}}\frac{\partial u_r}{\partial r} + \hat{\mathbf{r}}\frac{\partial^2 u_z}{\partial r \partial z} + \hat{\mathbf{z}}\frac{\partial^2 u_r}{\partial r \partial z} + \frac{1}{r}\hat{\mathbf{z}}\frac{\partial u_r}{\partial z} + \hat{\mathbf{z}}\frac{\partial^2 u_z}{\partial z^2}\right] = 0. \tag{5}$$

Moreover these displacement fields lead to the following stresses:

$$\sigma_{rr} = (\lambda + 2\mu)\frac{\partial u_r}{\partial r} + \lambda\frac{1}{r}u_r + \lambda\frac{\partial u_z}{\partial z} \tag{6}$$

$$\sigma_{rz} = \mu\left(\frac{\partial u_z}{\partial r} + \frac{\partial u_r}{\partial z}\right) \tag{7}$$

$$\sigma_{zz} = (\lambda + 2\mu)\frac{\partial u_z}{\partial z} + \lambda\left(\frac{\partial u_r}{\partial r} + \frac{1}{r}u_r\right). \tag{8}$$

The special form of the components u_r, u_z underlies the specific features of the problem. We mention here the model suggested by Christensen in [37], constructed in order to study the effective uniaxial modulus of cylindrical composites with perfect interfaces. In that model the radial components of the displacement fields are assumed z-independent while the corresponding axial components are linear functions of the longitudinal dimension. This simple model can not support the current case of imperfect interfaces since the implication of shear stresses over the interface requires full dependence of the elastic fields on the coordinates of the structure. So the first fundamental suggestion of the present work is the adoption of extended representations for the elastic fields permitting the incorporation of the interfacial property, denoted by the stiffness coefficient ξ, as a crucial parameter of the problem. More precisely we adopt the representations $u_r = B(r)f(z)$, $u_z = A(r)g(z)$ in Eq. (5) and after some extended manipulations we conclude to

$$\mu\left[\frac{\hat{\mathbf{r}}}{r}\frac{\partial}{\partial r}(rB'(r))f(z) + f''(z)B(r)\hat{\mathbf{r}} - \frac{1}{r^2}\hat{\mathbf{r}}B(r)f(z) + \hat{\mathbf{z}}\frac{1}{r}\frac{\partial}{\partial r}(rA'(r))g(z) + A(r)g''(z)\right]$$
$$+ (\lambda + \mu)\left[\hat{\mathbf{r}}B''(r)f(z) - \frac{\hat{\mathbf{r}}}{r^2}B(r)f(z) + \frac{1}{r}\hat{\mathbf{r}}B'(r)f(z) + \hat{\mathbf{r}}A'(r)g'(z)\right.$$
$$\left. + \hat{\mathbf{z}}B'(r)f'(z) + \frac{1}{r}\hat{\mathbf{z}}B(r)f'(z) + \hat{\mathbf{z}}A(r)g''(z)\right] = 0. \tag{9}$$

Separating radial and axial components we acquire the differential system

$$\mu\left[\frac{1}{r}(rB'(r))'f(z) + f''(z)B(r) - \frac{1}{r^2}B(r)f(z)\right]$$
$$+ (\lambda + \mu)\left[B''(r)f(z) - \frac{1}{r^2}B(r)f(z) + \frac{1}{r}B'(r)f(z) + A'(r)g'(z)\right] = 0 \tag{10}$$

and

$$\mu\left[\frac{1}{r}(rA'(r))'g(z) + A(r)g''(z)\right]$$

$$+ (\lambda+\mu)\left[B'(r)f'(z) + \frac{1}{r}B(r)f'(z) + A(r)g''(z)\right] = 0. \qquad (11)$$

The solvability of this system for every possible coordinate pair (r,z) necessitates the assumption

$$f(z) = g(z) = e^{\kappa z}, \qquad (12)$$

which physically reflects the modeling of the attenuation of the underlying physical fields along the main axis of the composite material. Thus the attenuation rate κ is connected with the characteristic length L of the composite and ensures the situation of anchoring at $z = -L$. The differential system is transformed as follows:

$$(\lambda+2\mu)\left[B''(r) + \frac{1}{r}B'(r) - \frac{1}{r^2}B(r)\right] + \mu\kappa^2 B(r) + \kappa(\lambda+\mu)A'(r) = 0 \qquad (13)$$

and

$$A''(r) + \frac{1}{r}A'(r) + \frac{\lambda+2\mu}{\mu}\kappa^2 A(r) + \frac{\lambda+\mu}{\mu}\kappa\left[B'(r) + \frac{1}{r}B(r)\right] = 0. \qquad (14)$$

We differentiate the last equation with respect to r and obtain

$$A'''(r) - \frac{1}{r^2}A'(r) + \frac{1}{r}A''(r) + \frac{\lambda+2\mu}{\mu}\kappa^2 A'(r)$$

$$+ \frac{\lambda+\mu}{\mu}\kappa\left[B''(r) + \frac{1}{r^2}B(r) + \frac{1}{r}B'(r)\right] = 0. \qquad (15)$$

Using Eq. (13) we find that

$$A'''(r) - \frac{1}{r^2}A'(r) + \frac{1}{r}A''(r) + \frac{\lambda+2\mu}{\mu}\kappa^2 A'(r)$$

$$+ \frac{\lambda+\mu}{\mu}\kappa[\mu\kappa^2 B(r) + (\lambda+\mu)\kappa A'(r)]\left(-\frac{1}{\lambda+2\mu}\right) = 0, \qquad (16)$$

which after multiplication by r becomes

$$rA'''(r) - \frac{1}{r}A'(r) + A''(r)$$

$$+ \left[\frac{\lambda+2\mu}{\mu} - \left(\frac{(\lambda+\mu)^2}{\mu}\right)\left(\frac{1}{\lambda+2\mu}\right)\right]\kappa^2 rA'(r) - \left(\frac{\lambda+\mu}{\lambda+2\mu}\right)\kappa^3 rB(r) = 0. \qquad (17)$$

Differentiating and dividing by r we obtain

$$rA^{(iv)}(r) + \frac{1}{r}A'(r) + A'''(r) + \frac{1}{r^3}A'(r) - \frac{1}{r^2}A''(r) + \frac{1}{r}A'''(r)$$

$$+ \left[\frac{\lambda+2\mu}{\mu} - \left(\frac{(\lambda+\mu)^2}{\mu}\right)\left(\frac{1}{\lambda+2\mu}\right)\right]\kappa^2\left(\frac{1}{r}A'(r) + A''(r)\right)$$

$$- \left(\frac{\lambda+\mu}{\lambda+2\mu}\right)\kappa^3\left(B'(r) + \frac{1}{r}B(r)\right) = 0. \qquad (18)$$

We eliminate now $B(r)$ by combining the last equation with Eq. (14) and arrive at

$$A^{(iv)}(r) + \frac{2}{r}A'(r) + \frac{1}{r^3}A'(r) - \frac{1}{r^2}A''(r)$$

$$+ \left[\frac{\lambda+2\mu}{\mu} - \left(\frac{(\lambda+\mu)^2}{\mu}\right)\left(\frac{1}{\lambda+2\mu}\right)\right]\kappa^2\left(\frac{1}{r}A'(r) + A''(r)\right)$$

$$+ \left(\frac{\mu}{\lambda+2\mu}\right)\kappa^2\left(A''(r) + \frac{1}{r}A'(r) + \kappa^2 A(r)\right)$$

$$+ \left(\frac{\lambda+\mu}{\lambda+2\mu}\right)\kappa^4 A(r) = 0. \qquad (19)$$

We multiply with r^4, arrange terms and obtain the differential equation of fourth order:

$$r^4 A^{(iv)}(r) + 2r^3 A'''(r) + rA'(r) - r^2 A''(r) + 2(\kappa r)^2\left[rA'(r) + r^2 A''(r)\right]$$

$$+ (\kappa r)^4 A(r) = 0 \qquad (20)$$

The preceding differential equation would be a relatively simple Euler-type equation in the absence of attenuation (i.e in the case $k = 0$ corresponding to Christensen's model). However taking into account the parameter k leads to an extended order Bessel-type differential equation. The analytical handling of this differential equation is demanding and out of the scope of this particular work. The outcome of this analysis involves construction of the basis set for the solutions of the differential equation. Every solution can be represented via the following basis set:

$$A \in \{\kappa r J_1(\kappa r), \kappa r Y_1(\kappa r), f_1(\kappa r), f_2(\kappa r)\} \qquad (21)$$

where J_1 and Y_1 are the well known Bessel functions and f_j, $j = 1, 2$ stand for the special functions

$$f_1(\kappa r) = \left[\pi\kappa r J_0(\kappa r)J_1(\kappa r)Y_0(\kappa r) + \pi\kappa r Y_1(\kappa r) + \pi\kappa r (J_1)^2 Y_1(\kappa r)\right.$$

$$\left. - \pi\kappa r Y_1(\kappa r)\,_1 F_2\left(\frac{1}{2}; 1, 2; -(\kappa r)^2\right)\right] \qquad (22)$$

$$f_2(\kappa r) = \left[-\pi\kappa J_1(\kappa r) - \pi\kappa r J_0(\kappa r)Y_0(\kappa r)Y_1(\kappa r)\right.$$

$$- \pi\kappa r J_1(\kappa r)(Y_1(\kappa r))^2 + \pi\kappa r J_1(\kappa r)\,_1 F_2\left(\frac{1}{2}; 1, 2; -(\kappa r)^2\right)$$

$$\left. + 2\sqrt{\pi}J_1(\kappa r)G_{2,1}^{3,0}\left(\kappa r, \frac{1}{2}\bigg|\begin{matrix},&,&0,1\\-\frac{1}{2},&\frac{1}{2},\frac{1}{2},&0\end{matrix}\right)\right] \qquad (23)$$

The term $_1 F_2\left(\frac{1}{2}; 1, 2; -(\kappa r)^2\right)$ stands for the arbitrary generalized hypergeometric functions while Meijer G-function term is $G_{2,1}^{3,0}$.

After the radial components $A(r)$ are determined, we employ (14) in order to determine the functions $B(r)$. More precisely it holds that

$$B'(r) + \frac{1}{r}B(r) = -\kappa A(r) - \frac{\mu}{\kappa(\lambda+\mu)}\left[A''(r) + \frac{1}{r}A'(r) + \kappa^2 A(r)\right] \qquad (24)$$

and so

$$B(r) = \frac{\Gamma}{\kappa r} + g(\kappa r) \qquad (25)$$

where Γ is an integration constant and

$$g(\kappa r) = -\frac{1}{\kappa r}\int_0^{\kappa r} zA(z)dz$$

$$- \frac{\mu}{\lambda+\mu}\left(\frac{1}{\kappa r}\right)\int_0^{\kappa r}[zA''(z) + A'(z) + zA(z)]dz. \qquad (26)$$

Selecting each one of the members $A(r)$ of the family (21) we obtain one of the four independent solutions that generate every possible function $B(r)$. So working successively with the members $\kappa r J_1(\kappa r)$, $\kappa r Y_1(\kappa r)$, $f_1(\kappa r)$ and $f_2(\kappa r)$ we produce via representation (26) the elements $g_l(\kappa r)$, $l = -1, -2, 1, 2$.

Thus we are in position to represent the matrix and fiber fields in terms of the constructed basis solutions. We pay attention on the fact that only the members $(zJ_1, f_1(z))$ and $(g_{-1}, g_1(z))$ from the two families correspond to regular displacements and stresses at $r = 0$ and so are adequate to represent interior fields. The matrix fields require all the basis solutions to be expanded. We mention that the analytical method encountered in the present work creates the suitable framework to support every possible axial stress. The ideal case could be to apply a constant axial stress on the matrix portion of the composite and leave the fiber unstressed. This situation would allow the appearance of axial shearing, which plays the central role to the classification of the interface quality. However there is a price to pay if someone imposes rigorously an arbitrary axial loading, especially discontinuous as the aforementioned ideal axial loading. In that case

the spectral analysis followed throughout the paper for a specific value of the axial parameter κ should be repeated for a denumerable sequence of spectral parameters κ_n, $n = 1, 2, 3, \ldots$ as these values emerge from the inherent separation of variables technique. This is very reminiscent of the Fourier series technique followed in order to approximate discontinuous functions. So in that case, the numerical process described later, should be performed several times till the acquisition of a satisfactory convergence in the expansions of the underlying fields. We have made several computer experiments to this direction and verified a large augmentation in the numerical perplexity as well as the deterioration of the simple features of the method. Instead of that, we work only with a specific value of κ, produced at the first stage of the numerical investigation and incorporating the physical condition of anchoring. via this mechanism the value κ is interrelated with the axial dimension L of the composite. Restricting ourselves only to this particular value of the spectral variable κ, we gain in efficiency while the method is proved a posteriori to provide with an axial loading, which is a very good mollification of the real stimulus state. With these remarks in mind, we arrive at the following representations for the displacement fields:

$$u_z^f = [(\kappa r)\widetilde{A}_f J_1(\kappa r) + \widetilde{B}_f f_1(\kappa r)]e^{\kappa z} \tag{27}$$

$$u_r^f = \left[\widetilde{A}_f g_{-1}^f(\kappa r) + \widetilde{B}_f g_1^f(\kappa r)\right]e^{\kappa z} \tag{28}$$

$$u_z^m = [(\kappa r)\widetilde{A}_m J_1(\kappa r) + \widetilde{B}_m f_1(\kappa r) + (\kappa r)\widetilde{C}_m Y_1(\kappa r) + \widetilde{D}_m f_2(\kappa r)]e^{\kappa z} \tag{29}$$

$$u_r^m = \left[\frac{\widetilde{\Gamma}_m}{\kappa r} + \widetilde{A}_m g_{-1}^m(\kappa r) + \widetilde{B}_m g_1^m(\kappa r) + \widetilde{C}_m g_{-2}^m(\kappa r) + \widetilde{D}_m g_2^m(\kappa r)\right]e^{\kappa z} \tag{30}$$

where we recognize several arbitrary expansion coefficients. As usual these coefficients are going to be determined via the investigation of the several boundary and transmission conditions which the fields obey.

Referring to the interface, we mention that the radial displacements must be continuous there. This assumption leads to the first transmission condition

$$u_r^m|_{r=a^+} = u_r^f|_{r=a^-} \tag{31}$$

which, after the exploitation of the representations ((28) and (30)) offers the relation

$$\widetilde{A}_f g_{-1}^f(\kappa a) + \widetilde{B}_f g_1^f(\kappa a) = \frac{\Gamma_m}{\kappa a} + \widetilde{A}_m g_{-1}^m(\kappa a) + \widetilde{B}_m g_1^m(\kappa a) + \widetilde{C}_m g_{-2}^m(\kappa a) + \widetilde{D}_m g_2^m(\kappa a). \tag{32}$$

The continuity of the radial stresses along the interface results in the second transmission condition

$$\sigma_{rr}^m|_{r=a^+} = \sigma_{rr}^f|_{r=a^-} \tag{33}$$

which expressed in terms of the expanded fields is restated as follows:

$$\lambda_f\left[\widetilde{A}_f g_{-1}^f(\kappa a) + \widetilde{B}_f g_1^f(\kappa a)\right] + (\lambda_f + 2\mu_f)(\kappa a)\left[\widetilde{A}_f \dot{g}_{-1}^f(\kappa a) + \widetilde{B}_f \dot{g}_1^f(\kappa a)\right]$$
$$+ \lambda_f(\kappa a)[\widetilde{A}_f(\kappa a)J_1(\kappa a) + \widetilde{B}_f f_1(\kappa a)]$$
$$= \lambda_m\left[\widetilde{A}_m g_{-1}^m(\kappa a) + \widetilde{B}_m g_1^m(\kappa a) + \widetilde{C}_m g_{-2}^m(\kappa a) + \widetilde{D}_m g_2^m(\kappa a)\right]$$
$$- 2\mu_m\frac{\Gamma_m}{\kappa a} + (\lambda_m + 2\mu_m)(\kappa a)\left[\widetilde{A}_m \dot{g}_{-1}^m(\kappa a) + \widetilde{B}_m \dot{g}_1^m(\kappa a) + \widetilde{C}_m \dot{g}_{-2}^m(\kappa a) + \widetilde{D}_m \dot{g}_2^m(\kappa a)\right]$$
$$+ \lambda_m(\kappa a)\left[(\kappa a)\widetilde{A}_m J_1(\kappa a) + \widetilde{B}_m f_1(\kappa a) + (\kappa a)\widetilde{C}_m Y_1(\kappa a) + \widetilde{D}_m f_2(\kappa a)\right] \tag{34}$$

where differentiation with respect to the full argument is denoted with dotted functions. We postpone for a while the examination of the remaining conditions on the interface involving the stiffness coefficient in order to give some extra emphasis on their role and we pay attention on the exterior surface of the composite structure.

More precisely, the exterior surface is stress free. So the radial stress vanishes, i.e.

$$\sigma_{rr}^m|_{r=b} = 0 \tag{35}$$

and so

$$\lambda_m\left[\widetilde{A}_m g_{-1}^m(\kappa b) + \widetilde{B}_m g_1^m(\kappa b) + \widetilde{C}_m g_{-2}^m(\kappa b) + \widetilde{D}_m g_2^m(\kappa b)\right]$$
$$- 2\mu_m\frac{\Gamma_m}{\kappa b} + (\lambda_m + 2\mu_m)(\kappa b)\left[\widetilde{A}_m \dot{g}_{-1}^m(\kappa b) + \widetilde{B}_m \dot{g}_1^m(\kappa b) + \widetilde{C}_m \dot{g}_{-2}^m(\kappa b) + \widetilde{D}_m \dot{g}_2^m(\kappa b)\right]$$
$$+ \lambda_m(\kappa b)\left[(\kappa b)\widetilde{A}_m J_1(\kappa b) + \widetilde{B}_m f_1(\kappa b) + (\kappa b)\widetilde{C}_m Y_1(\kappa b) + \widetilde{D}_m f_2(\kappa b)\right] = 0. \tag{36}$$

In addition the shear stress field is zero on $r = b$, i.e.

$$\sigma_{rz}^m|_{r=b} = 0 \tag{37}$$

leading to

$$\mu_m(\kappa b)\left[\widetilde{A}_m(J_1(\kappa b) + (\kappa b)\dot{J}_1(\kappa b)) + \widetilde{B}_m \dot{f}_1(\kappa b) + \widetilde{C}_m(Y_1(\kappa b) + (\kappa b)\dot{Y}_1(\kappa b)) + \widetilde{D}_m \dot{f}_2(\kappa b)\right]$$
$$+ \frac{\Gamma_m}{\kappa b} + \widetilde{A}_m g_{-1}^m(\kappa b) + \widetilde{B}_m g_1^m(\kappa b) + \widetilde{C}_m g_{-2}^m(\kappa b) + \widetilde{D}_m g_2^m(\kappa b)\right] = 0. \tag{38}$$

Returning to the interface, we first make the remark that the tangential stresses must be continuous:

$$\sigma_{rz}^m|_{r=a^+} - \sigma_{rz}^f|_{r=a^-} = 0 \tag{39}$$

leading to

$$\mu_m(\kappa a)\left[\widetilde{A}_m(J_1(\kappa a) + (\kappa a)\dot{J}_1(\kappa a)) + \widetilde{B}_m \dot{f}_1(\kappa a) + \widetilde{C}_m(Y_1(\kappa a) + (\kappa a)\dot{Y}_1(\kappa a))\right.$$
$$+ \widetilde{D}_m \dot{f}_2(\kappa a) + \frac{\Gamma_m}{\kappa a} + \widetilde{A}_m g_{-1}^m(\kappa a) + \widetilde{B}_m g_1^m(\kappa a) + \widetilde{C}_m g_{-2}^m(\kappa a) + \widetilde{D}_m g_2^m(\kappa a)\right]$$
$$- \mu_f(\kappa a)\left[\widetilde{A}_f(J_1(\kappa a) + (\kappa a)\dot{J}_1(\kappa a)) + \widetilde{B}_f \dot{f}_1(\kappa a) + \widetilde{A}_f g_{-1}^f(\kappa a) + \widetilde{B}_f g_1^f(\kappa a)\right] = 0. \tag{40}$$

The crucial point of a non perfect interface lies in the fact that the tangential displacement field is no longer continuous on the interface. The ensuing transmission condition involving the quality parameter ξ of the interface is based on the assumption that the common shear stress mentioned in the condition above compensates the displacement discontinuity via a Hooke's law relation as follows:

$$\sigma_{rz}^m|_{r=a^+} = \xi\left(u_z^m|_{r=a^+} - u_z^f|_{r=a^-}\right) \tag{41}$$

which is quantified through the condition

$$\mu_m(\kappa a)\left[\widetilde{A}_m(J_1(\kappa a) + (\kappa a)\dot{J}_1(\kappa a)) + \widetilde{B}_m \dot{f}_1(\kappa a) + \widetilde{C}_m(Y_1(\kappa a) + (\kappa a)\dot{Y}_1(\kappa a))\right.$$
$$+ \widetilde{D}_m \dot{f}_2(\kappa a) + \frac{\Gamma_m}{\kappa a} + \widetilde{A}_m g_{-1}^m(\kappa a) + \widetilde{B}_m g_1^m(\kappa a) + \widetilde{C}_m g_{-2}^m(\kappa a) + \widetilde{D}_m g_2^m(\kappa a)\right]$$
$$= \xi a\left[(\kappa a)\widetilde{A}_m J_1(\kappa a) + \widetilde{B}_m f_1(\kappa a) + (\kappa a)\widetilde{C}_m Y_1(\kappa a) + \widetilde{D}_m f_2(\kappa a)\right.$$
$$- \left(\kappa a)\widetilde{A}_f J_1(\kappa a) - \widetilde{B}_f f_1(\kappa a)\right]. \tag{42}$$

The boundary condition (41) is an efficient model implemented already by one of the authors in a few applications. For example, we mention here the reference [6] for a very good description of the functionality of the specific boundary condition. For interfaces of good quality the parameter ξ is considerably large and the balance implied by Eq. (41) forces the discontinuity of the shear displacements to disappear practically. For small values of ξ we need a considerable discontinuity of shear displacements in order to compensate the common shear stress and this quantifies the deficiency of the composite.

What remains is the implementation of the loading condition. According to the discussion made above, the loading supported by our methodology is a mollification of the real constant loading along the end face of the matrix alone. What we have to do is to prescribe the loading on the periphery $r = b$ as follows:

$$\sigma_{zz}^m|_{z=0}^{r=b} = \sigma_0 \tag{43}$$

or

$$(\lambda_m + 2\mu_m)\kappa\Big[(\kappa b)\widetilde{A}_m J_1(\kappa b) + \widetilde{B}_m f_1(\kappa b) + (\kappa b)\widetilde{C}_m Y_1(\kappa b) + \widetilde{D}_m f_2(\kappa b)\Big]$$
$$+ \lambda_m\kappa\Big[\widetilde{A}_m \dot{g}^m_{-1}(\kappa b) + \widetilde{B}_m \dot{g}^m_1(\kappa b) + \widetilde{C}_m \dot{g}^m_{-2}(\kappa b) + \widetilde{D}_m \dot{g}^m_2(\kappa b)$$
$$+ \widetilde{A}_m\Big(\frac{1}{\kappa r}\Big)g^m_{-1}(\kappa b) + \widetilde{B}_m\frac{1}{\kappa b}g^m_1(\kappa b) + \widetilde{C}_m\Big(\frac{1}{\kappa b}\Big)g^m_{-2}(\kappa b)$$
$$+ \widetilde{D}_m\Big(\frac{1}{\kappa b}\Big)g^m_2(\kappa b)\Big] = \sigma_0. \tag{44}$$

The specific value of σ_0 is not important since the problem leads to the linear adaptation of the underlying fields to the imposition of this load so that the definition of the effective modulus E_{11} (see below Eq. (49)) is independent naturally of the magnitude of σ_0, as expected in the framework of linear elasticity.

Collecting the above boundary and transmission conditions, we form the following linear-algebraic inhomogeneous system

$$\mathbb{A}\mathbf{x} = \mathbf{b} \tag{45}$$

where $\mathbf{x}$ contains the unknown expansion coefficients, i.e.

$$\mathbf{x} = [\widetilde{A}_f, \widetilde{B}_f, \widetilde{A}_m, \widetilde{B}_m, \widetilde{C}_m, \widetilde{D}_m, \widetilde{\Gamma}_m]^T, \tag{46}$$

and $\mathbb{A}$ is a 7×7 matrix involving the known special functions appearing in the conditions and whose elements $a_{i,j}$, $i, j = 1, 2, \ldots, 7$ are given in Appendix. The right hand side $\mathbf{b}$ is again a 7×1 vector having zero elements except the seventh position where the stimulus of the process makes its appearance ($b_7 = \sigma_0$).

Once the coefficients are determined, we are in position to determine the displacement and stress field throughout the structure. Then we are able to obtain the mean values of axial displacements and stresses along the cross section at $z = 0$. More precisely we introduce the quantities

$$\sigma_{mean} = \frac{2}{(\kappa a)^2}\int_0^{\kappa a}\left(\omega\sigma^f_{zz}|_{z=0}\right)d\omega + \frac{2}{(\kappa b)^2 - (\kappa a)^2}\int_{\kappa a}^{\kappa b}\left(\omega\sigma^m_{zz}|_{z=0}\right)d\omega \tag{47}$$

and

$$u^{mean}_z = \frac{2}{(\kappa a)^2}\int_0^{\kappa a}\left(\omega u^f_z(\omega)\right)d\omega + \frac{2}{(\kappa b)^2 - (\kappa a)^2}\int_{\kappa a}^{\kappa b}\left(\omega u^m_z(\omega)\right)d\omega \tag{48}$$

which participate in the formation of the uniaxial effective modulus E_{11} as follows:

$$E_{11} = \frac{\sigma_{mean}}{u^{mean}_z \kappa} \tag{49}$$

3. Numerical modeling

We have used the following parameters describing the physical system under investigation taken from experimental measurements [38]. For the SiC (SCS-6) fiber we consider a Young's modulus $E_f = 393$ GPa, and for the Ti–6Al–4V matrix which is ductile, a Young's mobulus $E_m = 110$ GPa. The SCS-6 (SiC) fiber is approximately 0.14 mm in diameter and the Ti–6Al–4V matrix is 1.4 mm. For the Poisson ratio's of SiC fiber we use $v_f = 0.32$ and for matrix Ti–6Al–4V $v_m = 0.18$. Lamé constants (λ, μ) can be obtained through the following equations

$$\lambda_w = \frac{E_w v_w}{(1 + v_w)(1 - 2v_w)} \tag{50}$$

and

$$\mu_w = \frac{E_w}{2(1 + v_w)} \tag{51}$$

with $w = f, m$ where f stands for fiber (SiC) and m for matrix (Ti–6Al–4V).

The starting point of the numerical investigation in the computer experiment is the adoption of the suitable geometrical parameter κ. As mentioned in the previous section the selection of the attenuation parameter κ decodes information about the axial dimension of the specimen and incorporates naturally the process of anchoring. The specification of κ has been performed through a suitable renormalization procedure. More precisely, we investigated first a pilot problem arising after the removal of the fiber component. In that case we determined the appropriate value of κ so that the effective uniaxial modulus restores the material's bulk modulus. In any case this value of κ is indicative of the length of the cylinder since it participates effectively in the exponential term $\exp(\kappa z)$, imposing the rate attenuation of the displacement along the composite and its practical vanishing occurs at the position of the anchoring mechanism. Providing this value of κ to the linear algebraic system Eq. (45), we proceed to its solution using LU-decomposition. The condition number of the constructed system varied from 10^4 to 10^6 indicative of a non-ill-posed problem [39–41] and the value of the residual norm of the error of the solution of the system was close to 10^{-16} for all cases studied. This numerical process is performed repeatedly for an extended region of bonding parameters ξ. Every numerical experiment leads to the calculation of the corresponding expansion coefficients $(\widetilde{A}_f, \widetilde{B}_f, \widetilde{A}_m, \widetilde{B}_m, \widetilde{C}_m, \widetilde{D}_m, \widetilde{\Gamma}_m)$, which afterwards determine everywhere throughout the structure the displacements and stresses. Finally we are able to obtain the mean values of axial displacements and stresses using Eqs. (47) and (48) along the cross section at $z = 0$. We conclude so to the formulation of the uniaxial effective modulus E_{11} as a function of ξ depicted in Fig. 2. The results shown in Fig. 2 clearly demonstrate the effect of interfacial property on the effective elastic property of the composite.

We mention here that the curves depicted in Fig. 2 give birth to suitable functions of the type $E_{11} = f(\xi)$. The evident monotonicity of the produced curves allows the inversion of this law providing the dependence $\xi = f^{-1}(E_{11})$. This is one of the main outcomes of the present work since it permits the characterization of the bond quality parameter ξ via the uniaxial effective modulus E_{11}, which is directly acquired by real experimental measurements. More precisely, measuring a value of E_{11} close to the right plateau critical value corresponds to the perfect interface case while measurements of the effective uniaxial modulus close to the left plateau region verify the undesirable total debonding of the structure. Intermediate values of E_{11} characterize the degree of the quality on the basis of Eq. (41) by estimating the relative shifting of the sizes of the interface under a specific axial load. In order to reveal the special features of this dependence we have first plotted the axial deformation of the cylinder, across its end face, for a couple of values of the parameter ξ as depicted in Figs. 3 and 4. In addition we have added a supplementary diagram figuring the dependence of the shearing displacement discontinuity across the interface on the quality parameter ξ (Fig. 5). This diagram indicates how discontinuity gives progressively place to continuity as the parameter ξ increases considerably.

We present numerical results for the real composite SiC fiber – Ti–6Al–4V matrix and for the test case composite where we have a SiC matrix and Ti–6Al–4V fiber. It is evident that the system having SiC fiber has higher effective moduli E_{11} values (ranging from 3.3×10^{11} Pa to 7.7×10^{11} Pa) compared to the composite with Ti–6Al–4V fiber (ranging from 1.28×10^{11} Pa to 2.85×10^{11} Pa) as it is anticipated. The dependence of effective moduli E_{11} on ξ follows the same shape and form regardless the fiber material. The effective moduli E_{11} exhibits two characteristic plateau regions distinct for low and high values of the interface quality parameter ξ for the systems studied. We should remind that high $\xi(\xi \to \infty)$ val-
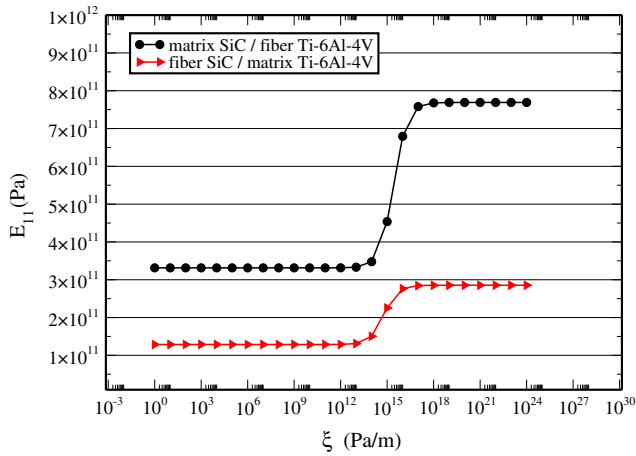
Fig. 2. Effective moduli E_{11} versus quality of the interface ξ. For Ti–6Al–4V matrix $\kappa = 1.145 \times 10^4 \, \text{m}^{-1}$ and for SiC matrix $\kappa = 1.164 \times 10^4 \, \text{m}^{-1}$.
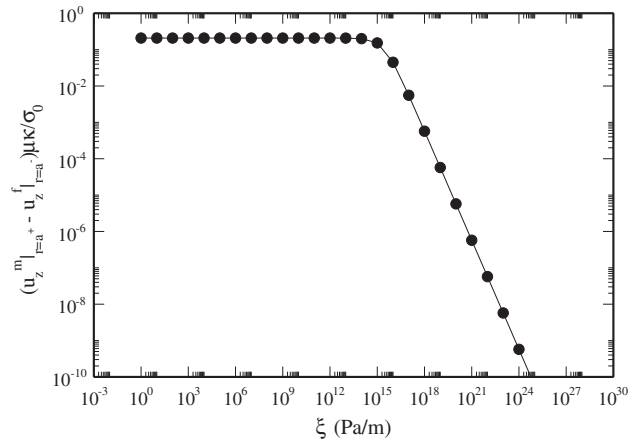

Fig. 5. Differential displacement on interface $\left(u_z^m|_{r=a^+} - u_z^f|_{r=a^-} \right)(\mu\kappa/s\sigma_0)$ as a function of the quality of the interface ξ.
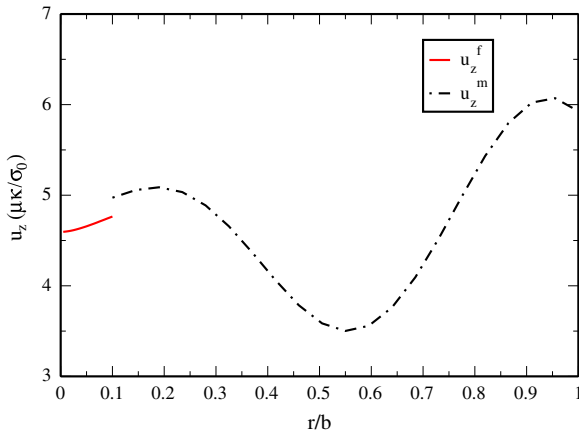

Fig. 3. Displacements versus normalized radius r/b for $\xi = 10^6$.
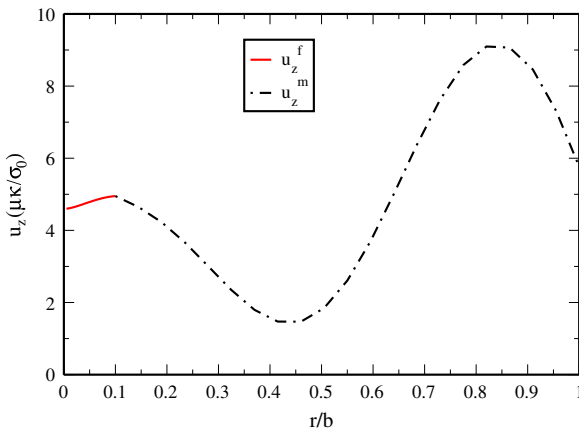

Fig. 4. Displacements versus normalized radius r/b for $\xi = 10^{18}$.

ues correspond to perfect interface where the displacement field is continuous. Small values of $\xi(\xi \to 0)$ refer to debonded interface where no transverse stress can be transferred from the one component to the other. For intermediate values of the interface quality parameter ξ we recognize an abrupt transition from the low

plateau E_{11} values regime to the high plateau E_{11} values regime giving birth to an intermediate neck type region. For the studied cases the aforementioned neck type region varies from $\xi = 10^{13}$ Pa/m to $\xi = 10^{16}$ Pa/m and represents the transition from poor to excellent interface quality. Although the starting value of ξ for the intermediate region is more or less identical for the two systems the composite having SiC fiber has the transition to the second plateau region shifted to higher ξ values.

4. Conclusions

A theoretical model accompanied with numerical simulation has been developed in this paper enabling estimation of interface elastic property in model single fiber composite systems subjected to tensile loading. The model geometry was a cylindrical composite structure (matrix–fiber) assumed to be homogeneous, isotropic with elastic materials characterized by Lamé constants λ, μ and density ρ. We developed an efficient mathematical model starting from the static linearized equation of elasticity and allowing relative transverse displacement shifting across the interface. For uniaxial loading following the proper analytical decomposition, and by proposing a new model for the displacement fields, it is possible to represent the elastic fields. This representation of elastic fields invokes unknown expansion coefficients that can be calculated as unknowns of a linear system, offered by the boundary conditions of the problem. Once the coefficients are determined, we were in position to calculate the displacement and stress fields throughout the structure. Then we were able to obtain the mean values of axial displacements and stresses along the cross section at $z = 0$ characterizing so the quality of the interface via the suitable exploitation of specific measurements.

Using this theoretical mathematical basis we were able to simulate a specific loading process applying a symmetric axial tension on the composite and study the produced effective uniaxial modulus E_{11} as a function of the quality of the interface ξ. The results clearly demonstrate the effect of interfacial property on the effective elastic property of the composite. The effective moduli E_{11} exhibits two characteristic plateau regions for the low and high values of the interface quality parameter ξ for the systems studied. For intermediate values of the interface quality parameter ξ we recognize an abrupt transition from the low plateau E_{11} values regime to the high plateau E_{11} values regime giving birth to an intermediate neck type region. Our suggested methodology provides in any case the aforementioned functional relation $\xi = f^{-1}(E_{11})$ allowing the non-destructive evaluation of the interface quality param-

eter ξ via experimental measurements of uniaxial effective modulus E_{11}. Further exploitation of the inversion can been implemented via the diagram of Fig. 5, which provides with estimations of the axial displacement discontinuity across the interface with respect to the value of the interfacial strength/stiffness parameter.

Acknowledgments

Appendix A

The elements of the matrix $\mathbb{A}$ are:

$$a_{11} = g^f_{-1}(\kappa a)$$

$$a_{12} = g^f_1(\kappa a)$$

$$a_{13} = -g^m_{-1}(\kappa a)$$

$$a_{14} = -g^m_1(\kappa a)$$

$$a_{15} = -g^m_{-2}(\kappa a)$$

$$a_{16} = -g^m_2(\kappa a)$$

$$a_{17} = -\frac{1}{\kappa a}$$

$$a_{21} = \lambda_f g^f_{-1}(\kappa a) + (\lambda_f + 2\mu_f)(\kappa a)\dot{g}^f_{-1}(\kappa a) + \lambda_f(\kappa a)^2 J_1(\kappa a)$$

$$a_{22} = \lambda_f g^f_1(\kappa a) + (\lambda_f + 2\mu_f)(\kappa a)\dot{g}^f_1(\kappa a) + \lambda_f(\kappa a)f_1(\kappa a)$$

$$a_{23} = -\lambda_m g^m_{-1}(\kappa a) - (\lambda_m + 2\mu_m)(\kappa a)\dot{g}^m_{-1}(\kappa a) - \lambda_m(\kappa a)^2 J_1(\kappa a)$$

$$a_{24} = -\lambda_m g^m_1(\kappa a) - (\lambda_m + 2\mu_m)(\kappa a)\dot{g}^m_1(\kappa a) - \lambda_m(\kappa a)f_1(\kappa a)$$

$$a_{25} = -\lambda_m g^m_{-2}(\kappa a) - (\lambda_m + 2\mu_m)(\kappa a)\dot{g}^m_{-2}(\kappa a) - \lambda_m(\kappa a)^2 Y_1(\kappa a)$$

$$a_{26} = -\lambda_m g^m_2(\kappa a) - (\lambda_m + 2\mu_m)(\kappa a)\dot{g}^m_2(\kappa a) - \lambda_m(\kappa a)f_1(\kappa a)$$

$$a_{27} = \frac{2\mu_m}{\kappa a}$$

$$a_{31} = 0$$

$$a_{32} = 0$$

$$a_{33} = \lambda_m g^m_{-1}(\kappa b) + (\lambda_m + 2\mu_m)(\kappa b)\dot{g}^m_{-1}(\kappa b) + \lambda_m(\kappa b)^2 J_1(\kappa b)$$

$$a_{34} = \lambda_m g^m_1(\kappa b) + (\lambda_m + 2\mu_m)(\kappa b)\dot{g}^m_1(\kappa b) + \lambda_m(\kappa b)f_1(\kappa b)$$

$$a_{35} = \lambda_m g^m_{-2}(\kappa b) + (\lambda_m + 2\mu_m)(\kappa b)\dot{g}^m_{-2}(\kappa b) + \lambda_m(\kappa b)^2 Y_1(\kappa b)$$

$$a_{36} = \lambda_m g^m_2(\kappa b) + (\lambda_m + 2\mu_m)(\kappa b)\dot{g}^m_2(\kappa b) + \lambda_m(\kappa b)f_2(\kappa b)$$

$$a_{37} = -\frac{2\mu_m}{\kappa b}$$

$$a_{41} = 0$$

$$a_{42} = 0$$

$$a_{43} = \mu_m(\kappa b)\left(J_1(\kappa b) + (\kappa b)\dot{J}_1(\kappa b) + g^m_{-1}(\kappa b)\right)$$

$$a_{44} = \mu_m(\kappa b)\left(\dot{f}_1(\kappa b) + g^m_1(\kappa b)\right)$$

$$a_{45} = \mu_m(\kappa b)\left(Y_1(\kappa b) + (\kappa b)\dot{Y}_1(\kappa b) + g^m_{-2}(\kappa b)\right)$$

$$a_{46} = \mu_m(\kappa b)\left(\dot{f}_2(\kappa b) + g^m_2(\kappa b)\right)$$

$$a_{47} = \mu_m$$

$$a_{51} = -\mu_f(\kappa a)\left(J_1(\kappa a) + (\kappa a)\dot{J}_1(\kappa a) + g^f_{-1}(\kappa a)\right)$$

$$a_{52} = -\mu_f(\kappa a)\left(\dot{f}_1(\kappa a) + g^f_1(\kappa a)\right)$$

$$a_{53} = \mu_m(\kappa a)\left(J_1(\kappa a) + (\kappa a)\dot{J}_1(\kappa a) + g^m_{-1}(\kappa a)\right)$$

$$a_{54} = \mu_m(\kappa a)\left(\dot{f}_1(\kappa a) + g^m_1(\kappa a)\right)$$

$$a_{55} = \mu_m(\kappa a)\left(Y_1(\kappa a) + (\kappa a)\dot{Y}_1(\kappa a) + g^m_{-2}(\kappa a)\right)$$

$$a_{56} = \mu_m(\kappa a)\left(\dot{f}_2(\kappa a) + g^m_2(\kappa a)\right)$$

$$a_{57} = \mu_m$$

$$a_{61} = \xi a^2 J_1(\kappa a)$$

$$a_{62} = \xi a f_1(\kappa a)$$

$$a_{63} = \mu_m(\kappa a)\left(J_1(\kappa a) + (\kappa a)\dot{J}_1(\kappa a) + g^m_1(\kappa a)\right) - \xi a(\kappa a J_1(\kappa a))$$

$$a_{64} = \mu_m(\kappa a)\left(\dot{f}_1(\kappa a) + g^m_1(\kappa a)\right) - \xi a f_1(\kappa)$$

$$a_{65} = \mu_m(\kappa a)\left(Y_1(\kappa a) + (\kappa a)\dot{Y}_1(\kappa a) + g^m_2(\kappa a)\right) - \xi a(\kappa a Y_1(\kappa a))$$

$$a_{66} = \mu_m(\kappa a)\left(\dot{f}_2(\kappa a) + g^m_2(\kappa a)\right) - \xi a f_2(\kappa)$$

$$a_{67} = \mu_m$$

$$a_{71} = 0$$

$$a_{72} = 0$$

$$a_{73} = (\lambda_m + 2\mu_m)(\kappa^2 b)J_1(\kappa b) + \lambda_m \kappa \left(\dot{g}^m_{-1}(\kappa b) + \frac{1}{\kappa b}g^m_{-1}(\kappa b)\right)$$

$$a_{74} = (\lambda_m + 2\mu_m)(\kappa)f_1(\kappa b) + \lambda_m \kappa \left(\dot{g}^m_1(\kappa b) + \frac{1}{\kappa b}g^m_1(\kappa b)\right)$$

$$a_{75} = (\lambda_m + 2\mu_m)(\kappa^2 b)Y_1(\kappa b) + \lambda_m \kappa \left(\dot{g}^m_{-2}(\kappa b) + \frac{1}{\kappa b}g^m_{-2}(\kappa b)\right)$$

$$a_{76} = (\lambda_m + 2\mu_m)(\kappa)f_2(\kappa b) + \lambda_m \kappa \left(\dot{g}^m_2(\kappa b) + \frac{1}{\kappa b}g^m_2(\kappa b)\right)$$

$$a_{77} = 0$$

References

[1] Metcalfe AG. Interfaces in metal matrix composites. New York: Academic Press; 1974.
[2] Shaw LL, Matikas TE, Karpur P, Hu S, Miracle DB. Fracture strength and damage progression of the fiber/matrix interfaces in titanium-based MMCS with different interfacial layers. Compos Part B: Eng 1998;29:331–9.
[3] Soulioti DV, Aggelis DG, Barkoula NM, Paipetis A, Matikas TE, Shiotani T. Acoustic emission behavior of steel fibre reinforced concrete under bending. Constr Build Mater 2009;23:3532–6.
[4] Clyne TW, Feillard P, Kalton A. Interfacial mechanics and macroscopic failure in titanium-based composites. In: ASTM symposium on life prediction methodology for titanium matrix composites, vol. 28; 1994. p. 185–201.
[5] Ghosn LJ, Eldridge JI, Kantzos P. Analytical modeling of the interfacial stress state during pushout testing of SCS-6/Ti-based composites. Acta Metall 1994;42:3895–908.
[6] Karpur P, Matikas TE, Krishnamurthy S. Ultrasonic characterization of the fiber–matrix interphase/interface for mechanics of continuous fiber reinforced metal matrix and ceramic matrix composites. Compos Eng 1995;5:697–711.
[7] Warrier SG, Majumdar BS, Gundel DB, Miracle DB. Implications of tangential shear failure during transverse loading of metal matrix composites. Acta Metall 1997;45:3469–80.
[8] Miracle DB, Gundel DB, Warrier SG. Interfacial structure and properties for the design of fiber-reinforced metal matrix composites. PA: Academic Press; 1996.
[9] Kelly A, Tyson WR. Tensile properties of fiber-reinforced metals: copper/tungsten and copper/molybdenum. J Mech Phys Solids 1965;3:329–50.
[10] Favre J-P, Jacques D. Stress transfer in carbon fibre model composites. J Mater Sci 1990;25:1373–80.
[11] Waterbury MC, Drzal LT. On the determination of fiber strengths by in-situ fiber strength testing. J Compos Tech Res 1991;13:22–8.
[12] Narkis M, Chen EJH, Pipes RB. Review of methods for characterization of interfacial fiber–matrix interactions. Polym Compos 1988;9:245–51.
[13] Henstenburg RB, Phoenix SL. Interfacial shear strength studies using the single-filament composite test. Part II: A probability model and Monte Carlo simulation. Polym Compos 1989;10:389–408.
[14] Drzal LT, Rich M, Lloyd P. Adhesion of graphite fibers to epoxy matrices. I. The role of fiber surface treatment. J Adhes 1983;16:1–30.

[15] Fraser WA, Ancker FH, DiBenedetto AT, Elbirli B. Evaluation of surface treatments for fibers in composite materials. Polym Compos 1983;4: 238–48.

[16] Netravali AN, Henstenburg RB, Phoenix SL, Schwartz P. Interfacial shear strength studies using the single-filament-composite test. Part I: Experiments on graphite fibers in epoxy. Polym Compos 1989;10:226–41.

[17] Torres FG, Cubillas ML. Study of the interfacial properties of natural fibre reinforced polyethylene. Polym Testing 2005;24:694–8.

[18] Li X-M, Wang J-H, Gao G-Q, Feng W. Study on the interfacial adhesion conditions by single-fiber composite fragmentation test. Wuhan Ligong Daxue Xuebao/J Wuhan Univ Technol 2005;27:9–12.

[19] Ochiai S, Osamura K. Multiple fracture of a fibre in a single tungsten fibre–copper matrix composite. Z Metallkd 1986;77:255–9.

[20] Roman I, Aharonov R. Mechanical interrogation of interfaces in monofilament model composites of continuous SiC fiber–aluminium matrix. Acta Metall Mater 1992;40:477–85.

[21] Molliex L, Favre J-P, Vassel A, Rabinovitch M. Interface contribution to the SiC–titanium and SiC–aluminium tensile strength prediction. J Mater Sci 1994;29:6033–40.

[22] Matikas T, Nicolaou PD. Development of a model for the prediction of the fretting fatigue regimes. J Mater Res 2001;16:2716–23.

[23] Clough RB, Biancaniello FS, Wadley HNG, Kattner UR. Fiber and interface fracture in single crystal aluminium/SiC fiber composites. Metall Trans 1990;21A:2747–57.

[24] Houpert J-L, Phoenix SL, Raj R. Analysis of the single-fiber-composite test to measure the mechanical properties of metal–ceramic interfaces. Acta Metall Mater 1994;42:4177–87.

[25] Vassel A, Merienne MC, Pautonnier F, Molliex L, Favre J-P. A method to evaluate the bonding between fibre and matrix in Ti-base composite. In: Lacombe P, Tricot R, Beranger G, editors. Proceedings of 6th world conference on titanium, Les Editions de Physique, Les Ulis Cedex, France, vol. 29; 1988. p. 919–23.

[26] Petitcorps YL, Pailler R, Naslain R. The fibre/matrix interfacial shear strength in titanium alloy matrix composites reinforced by silicon carbide or boron CVD filaments. Compos Sci Technol 1989;35:207–14.

[27] Favre J-P, Vassel A, Laclau C. Testing of sic/titanium composites by fragmentation and push-out tests: Comparison and discussion of test data. Composites 1994;25:482–7.

[28] Preuss M, Rauchs G, Withers PJ, Maire E, Buffiere J-Y. Interfacial shear strength of Ti/SiC fibre composites measured by synchrotron strain measurement. Composites Part A 2002;33:1381–5.

[29] Matikas TE, Rousseau M, Gatignol P. Theoretical analysis for the reflection of a focused ultrasonic beam from a fluid–solid interface. J Acoust Soc Am 1993;93:1407–16.

[30] Waterbury MC, Karpur P, Matikas TE, Krishnamurthy S, Miracle DB. In situ observation of the single fiber fragmentation process in metal matrix composites by ultrasonic imaging. Compos Sci Technol 1994;52:261–6.

[31] Karpur P, Benson DM, Matikas TE, Kundu T, Nicolaou PD. An approach to determine the experimental transmitter–receiver geometry for the reception of leaky lamb waves. Mater Eval 1995;53:1348–52.

[32] Matikas TE, Rousseau M, Gatignol P. Experimental study of focused ultrasonic beams reflected at a fluid–solid interface in the neighborhood of the rayleigh angle. Trans Ultrason Ferroelectr Freq Control 1992;39:737–44.

[33] Krishnamurthy S, Matikas TE, Karpur P, Miracle DB. Ultrasonic evaluation of the processing of fiber-reinforced metal–matrix composites. Compos Sci Technol 1995;54:161–8.

[34] Wu Z, Ye JQ, Cabrera J. 3d analysis of stress tranfer in the micromechanics of fiber reinforced composites by using an eigen-function expansion method. J Mech Phys Solids 2000;48:1037–63.

[35] Flugge W, Kelkar VS. The problem of an elastic circular cylinder. Int J Solids Struct 1968;4:397–420.

[36] Smith G, Spencer A. Interfacial reactions in a fibre-reinforced elastic composite material. J Mech Phys Solids 1970;18:81–100.

[37] Christensen R. Mechanics of composite materials. 2nd ed. Dover Publications Inc.; 2005.

[38] Frantziskonis GN, Karpur P, Matikas TE, Krishnamurthy S, Jero PD. Fiber–matrix interface: information from experiments via simulation. Compos Struct 1994;29:231–47.

[39] Gergidis LN, Kourounis D, Mavratzas S, Charalambopoulos A. Acoustic scattering in prolate spheroidal geometry via Vekua Tranformation – theory and numerical results. CMES: Comput Model Eng Sci 2007;21:157–75.

[40] Kourounis D, Gergidis LN, Charalambopoulos A. Sensitivity of the acoustic scattering problem in prolate spheroidal geometry with respect to wavenumber and shape. CMES: Comput Model Eng Sci 2008;28:185–201.

[41] Mavratzas S, Charalambopoulos A, Gergidis LN. Scattering from two eccentric spheroids: theory and numerical investigation. Int J Eng Sci 2010;48:174–87.